Journal of Porous Materials (2023) 30:1965–1974
https://doi.org/10.1007/s10934-023-01471-x

Mesoporous colloidal silica cubes with catalytically active cores

Alessio J. Sprockel[1] · Frans Dekker[1] · Remco Tuinier[2] · Albert P. Philipse[1]

Accepted: 30 April 2023 / Published online: 25 May 2023
© The Author(s) 2023

Abstract
Preparation methods of cubic core-shell particles with specific functionality are limited. Here we demonstrate the possibility to transform cuprous oxide cubes coated with mesoporous silica into functional core-shell particles, while retaining their cubic shape. Cuprous oxide nanocubes are coated with mesoporous silica using cetyltrimethylammonium bromide as a template, after which the cuprous oxide core is transformed using liquid phase calcination and galvanic replacement. Nitrogen physisorption and electron microscopy confirm that mesoporous silica coatings are obtained with tuneable thickness. The successful transformation of cuprous oxide into gold and silver is assessed via UV–VIS spectroscopy and energy dispersive X-ray spectroscopy. Particles with a silver core and a cubic mesoporous silica shell are demonstrated to be catalytically active in the degradation of the dye Congo red.

Graphical abstract

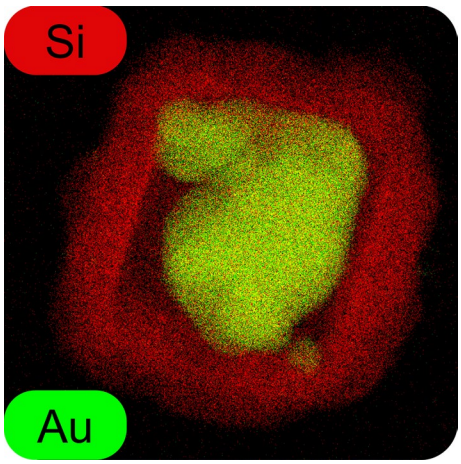

Keywords Core-shell · Cubic nanoparticles · Catalytic dye degradation · Cuprous oxide · Silica

1 Introduction

Colloidal cubes are able to form dense packings when assembled by gravity [1, 2], the depletion interaction [3], or confinement in 2D [4] and 3D [5, 6]. Cubic colloids can be prepared as noble metals [7–9], metal oxides [10, 11], and perovskites [12], all of which have properties depending on their detailed size, shape and chemistry. For applications it is desirable to combine the catalytic [8] or plasmonic properties [13] of nanomaterials with a specific shape, arranged in

✉ Alessio J. Sprockel
a.j.sprockel@uu.nl

[1] Van 't Hoff Laboratory for Physical and Colloid Chemistry, Debye Institute for Nanomaterials Science, Utrecht University, Padualaan 8, Utrecht 3584 CH, The Netherlands

[2] Laboratory of Physical Chemistry, Department of Chemical Engineering and Chemistry & Institute for Complex Molecular Systems, Eindhoven University of Technology, Eindhoven 5600 MB, The Netherlands

a crystal lattice which is only obtainable by assembling particles with a different shape. The formation of bicontinuous Pickering emulsions illustrates this point, as specific particle shape and surface chemistry are beneficial, but the inclusion of shape decoupled functionality is not yet achieved. [14, 15] A method commonly proposed to add functionality to particles, is the impregnation of porous materials with functional materials [16], sometimes referred to as the "ship-in-a-bottle approach" [17]. Although this approach allows to incorporate different functional materials in a carrier material, the product often has low specificity and a low fraction of filled particles [18]. Here we propose a different route towards the deposition of functional material into an anisotropic carrier material, using the morphology of silica on cuprous oxide cubic-core-shell particles [19]. By using a method that alters the core but does not affect the silica shell, it is possible to completely transform the cuprous-oxide to gold or silver, while maintaining the outer shape of the particles.

Core-shell particles, or hollow materials containing functional materials, have been the subject of various studies. Since these hierarchical and complex morphologies often have a large surface area, they are expected to find applications as catalysts, energy storage or drug carriers [20–23]. One method to obtain functional core-shell particles is the self-templating method [21], via which functional colloids with complex morphologies, including cubes [24] and plates [25], have been prepared. The self-templating method uses the nanoparticle as a template to obtain a core-shell particle and complete transformation often results in a different morphology of the particle [21]. Functional materials deposited in an inert carrier material, such as silica, allows for the complete transformation of the functional material while preserving the shape and stability provided by the silica shell. An example of transformation in a silica shell, is the etching and overgrowth procedure of gold nanorods coated with mesoporous silica [26, 27]. Using the etching and overgrowth method, it is possible to obtain rods with a tuneable surface plasmon resonance. Similar procedures could be used to transform cubic core-shell particles. However, preparation methods of cubic particles coated with mesoporous silica are limited [28–32] and to the best of our knowledge no reports have been presented yet on the transformation of functional materials inside mesoporous silica nanocubes. A mesoporous silica coating on functional cores provides stability while allowing free transport of molecules to the core [33, 34]. A common method to obtain mesoporous silica is by the deposition of silica in the presence of surfactants [35]. For instance, using cetyltrimethylammonium bromide (CTAB) micelles it is possible to obtain free standing mesoporous silica [36] or core-shell particles [37]. The CTAB template can afterwards be extracted by ion exchange [38] or calcination [36, 39] resulting in silica with mesoscale pores. Characteristic for mesoporous silica obtained from CTAB micelles are pores with a diameter of 2 nm and surface areas over 1000 $m^2\ g^{-1}$ [35].

The aim of the present work is to explore the coating of cuprous oxide cubes with a mesoporous silica shell and the subsequent transformation of the cuprous oxide core into a functional material while conserving the cubic mesoporous silica. First, we attempt coating cuprous oxide nanocubes [19, 40] with a mesoporous silica shell using the CTAB soft template. The formed shells are then characterized using TEM and nitrogen physisorption. Using a high-temperature boiling solvent, the silica shell can afterwards be calcined while simultaneously thermolyzing the cuprous oxide into metallic copper. Finally, using galvanic replacement, the copper core can be substituted by noble metals like silver or gold. The resulting particles are characterized with UV–VIS spectroscopy and energy dispersive X-ray spectroscopy. The functionality of the newly formed particles is assessed by the catalytic dye degradation of Congo red.

2 Experimental

2.1 Materials

L-ascorbic acid (Reagent grade), ammonium chloride (≥ 99.5%), Congo red (91 wt% dye), gold chloride trihydrate (99.9%), silver nitrate (99%), tetraethyl orthosilicate (TEOS, ≥ 99.0%), polyvinylpyrrolidone (PVP-55, average molar weight of 55 kDa) and trioctylphosphine oxide (TOPO, 99%) were obtained from Sigma-Aldrich. Cetyltrimethylammonium bromide (CTAB, ≥ 99%) was purchased from Acrös Organics, ethanol (Technical grade) from VWR, sodium hydroxide (≥ 99%) from Merck, and nitric acid (65% aqueous solution) from Emsure. All water used was purified using a Millipore apparatus (18.2 Ω•cm @ 25 °C).

2.2 Cuprous oxide cube synthesis

The Cu_2O cubic template was produced using a method developed in our group [19]. To a 500 mL 3-neck round-bottom flask equipped with reflux and dripping funnel, 223 g 1,5-pentanediol and 25.3 g PVP-55 were added. The reflux condenser and dripping funnel were connected to a N2/Vacuum Schlenk line. The mixture was vacuum flushed three times at room temperature, heated to 100 °C by oil bath and vacuum flushed three times. 5.2 g $Cu(acac)_2$ and 75 g 1,5-pentanediol were weighed in a 100 ml bottle and mixed by a combination of shaking and sonication. The $Cu(acac)_2$ mixture was transferred to the dripping funnel and flushed four times. The PVP-55 solution was heated to 200 °C and the $Cu(acac)_2$ mixture was added over 30 s aided by N_2 pressure. After 22 min, heating was discontinued, and the mixture was allowed to cool down to room temperature,

yielding a brown mixture. The product was collected with 500 ml acetone. The resulting sol was separated by centrifugation (3000 g, 2.5 h) and washed twice with ethanol by centrifugation (12,000 g, 30 min). Finally, the sample was dispersed in 50 mL ethanol.

2.3 Mesoporous shell synthesis

Cubic cuprous oxide core, mesoporous silica shell particles ($Cu_2O@mSiO_2$) were obtained by coating Cu_2O cubic template particles with silica according to a modified procedure from Jiang et al. [41]. Cu_2O particles (100 mg in 164 mL of ethanol) were added to a 500 mL round-bottom flask equipped with mechanical stirrer. Water (36 mL), TEOS (0.125 mL), and CTAB (0.2 g) were added to the nanocubes and the mixture was stirred and sonicated for 15 min. An aqueous sodium hydroxide solution (20 mM, 10 mL) was added over 10 min using a Gilson peristaltic pump. Sonication was continued for 2 h after which the reaction was stirred overnight. The particles were washed by centrifugation (12,000 g, 30 min) three times and finally dispersed in ethanol (5 mL).

2.4 Template removal

Template extraction was performed to obtain hollow mesoporous particles with a cubic void ($mSiO_2$ shells) by a method adapted from Deekamwong et al. [38]. To a 100 mL 2-neck round-bottom flask equipped with magnetic stirring and a reflux condenser, silica coated cubes (50 mg) and ethanol (35 mL) were added. Ammonium chloride (1.02 g) was added and the mixture was refluxed for 45 min. The mixture was allowed to cool down, yielding an aqua-coloured mixture. Water (33 mL) followed by a drop a nitric acid were added, resulting in a clear dispersion. The product was washed by centrifugation, first three times with water, followed by three times with ethanol (20,000 g, 40 min). Finally, the particles were dispersed in ethanol (5 mL).

2.5 Liquid phase calcination and cuprous oxide thermolysis

Liquid Phase Calcination (LPC) was performed in a high boiling point solvent, trioctylphosphine oxide (TOPO), under nitrogen atmosphere to obtain $Cu@mSiO_2$ particles. [39] TOPO (7.1 g) was heated to 60 °C in a 100 mL round-bottom flask equipped with reflux condenser and stir bar. Cuprous oxide cubes coated with mesoporous silica ($Cu_2O@mSiO_2$, 50 mg in 2.5 mL ethanol) were added to the liquified TOPO, followed by removal of the ethanol by heating under vacuum. The mixture was heated to 350 °C under nitrogen atmosphere, and allowed to react for 1 h, after which the mixture was cooled down to 100 °C. Water (25 mL) was added and the sample was washed by centrifugation with water, three times, and ethanol, three times. The mixture was finally dispersed in ethanol (50 mL).

2.6 Galvanic replacement

Galvanic replacement of copper into silver was done following a procedure adapted from Stewart et al. [42]. The $Cu@mSiO_2$ (0.4 mg) obtained from LPC was dispersed in water (0.5 mL) after which freshly prepared solution of ascorbic acid (0.5 mL, 1.16 M in water) was added. The mixture was vortexed for 10 s and directly washed by centrifugation (16,000 g, 10 min) with water twice, and then dispersed in water (0.5 mL). Silver nitrate (0.5 mL, 50 mM in water) was added, the mixture was vortexed for 10 s and then directly washed by centrifugation with water (twice) and ethanol (twice). Finally, the particles were dispersed in ethanol (5 mL). For the galvanic replacement of copper with gold, $HAuCl_4$ (0.5 mL, 25 mM in water) was added instead of the silver nitrate.

2.7 Catalytic dye degradation

Catalytic dye hydrogenation by $Ag@mSiO_2$ particles was demonstrated by degradation of Congo red. To water (9 mL) $Ag@mSiO_2$ particles were added (0.4 mL, 0.1 mg mL^{-1}). To this dispersion an aqueous Congo red solution (70 µL, 5 mM) was added. Freshly prepared sodium borohydride (0.5 mL, 1 M) was added to initiate the dye hydrogenation, and changes in colour were monitored visually and with UV–VIS, with time intervals of approximately six minutes. During the reaction gas bubbles develop on the surface of the cuvet, a baseline correction was performed to account for scattering caused by these bubbles. Two control experiments were performed, one with $mSiO_2$ particles (0.01 mL, 0.4 mg mL^{-1}) with $NaBH_4$ and Congo red, and one with $NaBH_4$ and Congo red in the absence of any particles.

2.8 Characterization

Transmission Electron Microscopy (TEM) was performed on a TecNAI 12 and TecNAI 20 electron microscope. Images were recorded on an SIS CCD Megaview II camera. Samples were prepared by diluting a drop of analyte in water and casting a drop of dilute analyte on a copper grid, followed by drying of the copper grid under a heating lamp. **Energy-dispersive X-ray spectroscopy** (EDX) maps were obtained from a FEI Talos F200X, with samples prepared on an aluminum grid. **Nitrogen physisorption** isotherms were obtained with a Micrometrics Tristar II plus. Prior to the measurements the samples were dried overnight at 250 °C.

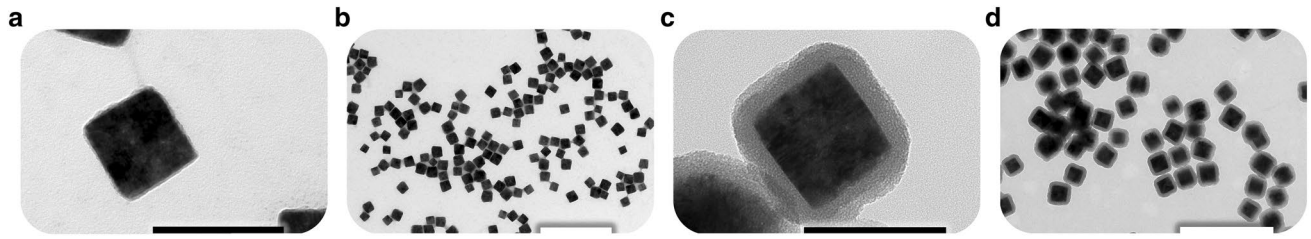

Fig. 1 **a b** TEM imaging of Cu_2O cubes, 92 ± 8 nm and **c d** Cu_2O@$mSiO_2$ cubes, 18 ± 2 nm silica. Scalebar 100 nm (white) and 500 nm (black)

The surface area was determined using the BET isotherm [43], and the micropore size distribution was determined using the BJH method assuming cylindrical pores. **UV–VIS** spectra were obtained using a PerkinElmer Lambda 35 UV-VIS spectrometer. Samples were measured in quartz cuvettes and the obtained spectra, ranging 250–700 nm, were normalized using Wolfram Mathematica. **IR** spectra were obtained using a PerkinElmer FT-IR/FIR Frontier spectrometer in transmission mode. 250 mg KBr with 1 mg sample was dried in a Memmert oven at 70 °C overnight. Copper core samples were dried under vacuum and nitrogen flow.

3 Results and discussion

3.1 Template synthesis and mesoporous coating

For coating with mesoporous silica (MCM-41) cuprous oxide cubes were synthesized with edge lengths of 96 ± 10 nm. MCM-41 silica is commonly prepared with ammonia as a base catalyst. Ammonia, however, dissolves the cuprous oxide core [44], which required us to find an alternative method. Using tetramethyl ammonium hydroxide as base catalyst results in non-uniform coatings, and adding TEOS to Cu_2O cubes with sodium hydroxide results in damaged cubes. By drop-wise addition of sodium hydroxide to the precursor mixture, it is possible to obtain cubes coated with mesoporous silica. Below, Cu_2O nanocubes are visible before (Fig. 1ab) and after (Fig. 1cd) coating, showing a lower contrast shell around the cubic core after the coating step.

Close up inspection of the obtained silica shells, Fig. 1c, reveals distinct features with sizes ranging between 2 and 4 nm. Similar to the microporous silica, the coating thickness can be controlled by increasing the amount of added TEOS (Fig. 2b). The main differences between Stöber silica coating previously studied in our group, [19] and the here explored mesoporous coating, are the thickness of the coating with respect to the TEOS/Cu_2O ratio, and the thickness of the coating at low amounts of added TEOS, visible in Fig. 2. For a given TEOS/Cu_2O ratio the mesoporous silica coatings are significantly thicker than for Stöber silica. This increased thickness is a direct result from the incorporated CTAB micelles in the coating, increasing the total volume of the silica shell. At low amounts of added TEOS, (below 1.20 µL/mg) the thickness drops down sharply, and suggests that adding less than 0.7 µL/mg TEOS would not result in a mesoporous coating. This is in contrast to the Stöber silica, where the data fit intersects the origin. [19] The reason for this difference can be attributed to the different reaction

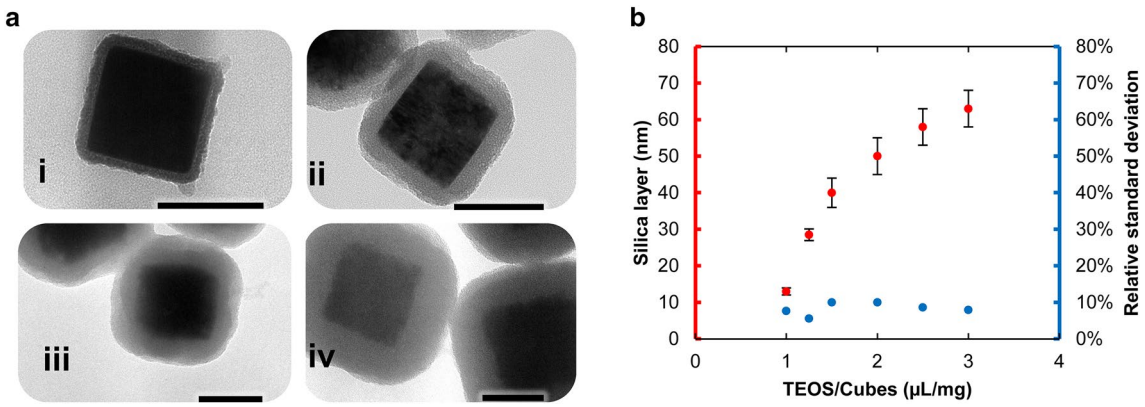

Fig. 2 **a** Cu_2O cubes coated with silica of an increasing layer thickness. Scale bar 100 nm. **b** After reaching a treshold concentration, silica coating thickness increases with TEOS addition. The normalized standard deviation in coating thickness stays below 10% for the entire range

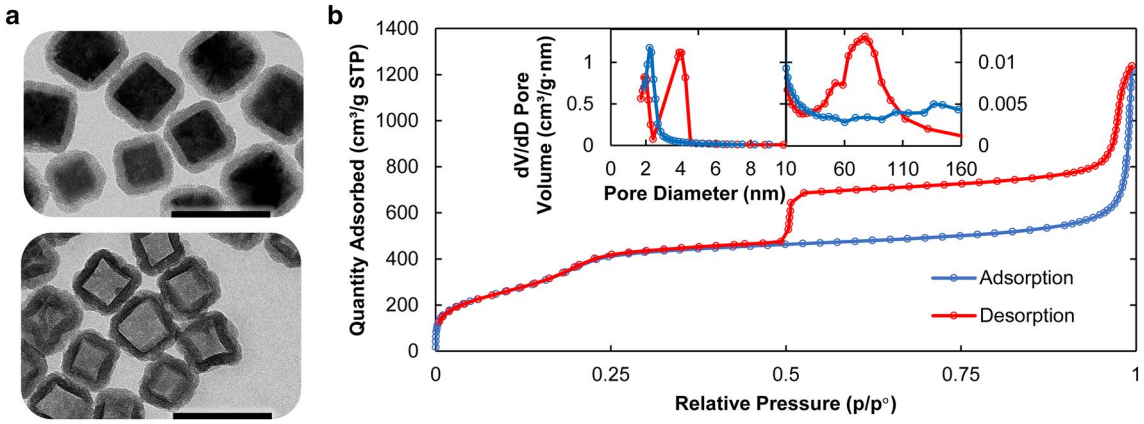

Fig. 3 **a** TEM imaging of cubes before and after removal of the cubic Cu_2O template by heating in ammonium chloride solution. Scale bar 200 nm. **b** Nitrogen physisorption isotherm for cubic void@$mSiO_2$ shells. The inset shows the dV/dD pore volume, with a characteristic pore size of 2–3 nm found in mesoporous silica prepared with CTAB

conditions. If instead of the layer thickness, the silica volume nm^3 is plotted, the trend is expected to be linear. This is the case above 1.5 µL/mg (TEOS/Cu_2O), and is shown in SI.1.

After extraction of the cuprous oxide template, the porosity of cubic mesoporous $mSiO_2$ shells was assessed with nitrogen physisorption (Fig. 3). In Fig. 3b, the N_2 physisorption isotherm of $mSiO_2$ shells is presented, showing a step increase at $p/p^0 \approx 0.2$, and a large hysteresis loop with sudden desorption at $p/p^0 \approx 0.5$, both typical for mesoporous materials [43]. The pore size distribution of $mSiO_2$ shells is depicted in the inset of Fig. 3b. From Fig. 3b it is apparent that mesopores are present in the silica obtained with CTAB, showing a distinct peak in the pore size distribution around 2 nm. This peak is not visible in the analysis of the nitrogen physisorption isotherm of Stöber silica shells (SI.2). The peak around 4 nm in de desorption curve is an artefact caused by meniscus instabilities, often observed in mesoporous materials [45]. Additionally, the $mSiO_2$ shells show a small peak in the desorption curve around 60–90 nm, which roughly corresponds with the size of the cubic void present in the hollow particles. The BET surface area was determined to be 1156 ± 17 m^2 g^{-1}. The density of the mesoporous silica was found to be 0.8 g/cm^3 by comparing the relative weight increase to the relative volume increase. This is in agreement with the 0.8 to 0.9 g/cm^3 found in literature. [46] Further insight into this calculation is given in SI.3.

3.2 Cuprous oxide transformation and galvanic replacement

Liquid phase calcination (LPC) [39] was used to calcine the cubic CuO_2@$mSiO_2$ particles while maintaining their colloidal stability. It was found that conventionally applied air calcination [36] resulted in aggregated particles that could not be dispersed in water or ethanol. During LPC of Cu_2O@$mSiO_2$ it was found that the calcination transformed the cuprous oxide core in a metallic copper core. This was earlier observed by Gao et al. for Cu_2O microcubes, who attributed the transformation to thermolysis [47]. After LPC, it is visible in Fig. 4a that the cubic cuprous oxide core evolves into a smaller rounded core, which is a result of the expulsion of oxygen. This transformation of the Cu_2O into metallic copper is also visible on IR and UV–VIS spectra. In Fig. 4b a clear decrease of the Cu-O stretching vibration at 650 cm^{-1} is visible after LPC, indicating the absence of cuprous oxide. Additionally, a decrease in O-H stretching and bending vibrations at 3500 cm^{-1} and 1650 cm^{-1}, respectively, is observed, indicating a loss of hydroxyl groups present in the particles. Furthermore, the UV–VIS spectra in Fig. 4c show a clear transformation from a typical Cu_2O spectrum (blue) [8] to the absorption spectrum of Cu (red) [48]. After LPC the particles could be dispersed in ethanol and regained stabilities comparable to before the calcination step, indicating the LPC method is a good way to calcine particles while retaining colloidal stability. In SI.4 TEM image are shown of samples taken during the LPC process, displaying the effects of the oxygen expulsion and subsequent surface melting.

Table 1 Half reaction standard potentials [49]

Half reaction	Standard Potential (V)
$Au^{3+}(aq) + 3e^- \rightarrow Au(s)$	1.498
$Ag^{+}(aq) + 1e^- \rightarrow Ag(s)$	0.7996
$Cu^{2+}(aq) + 2e^- \rightarrow Cu(s)$	0.3419

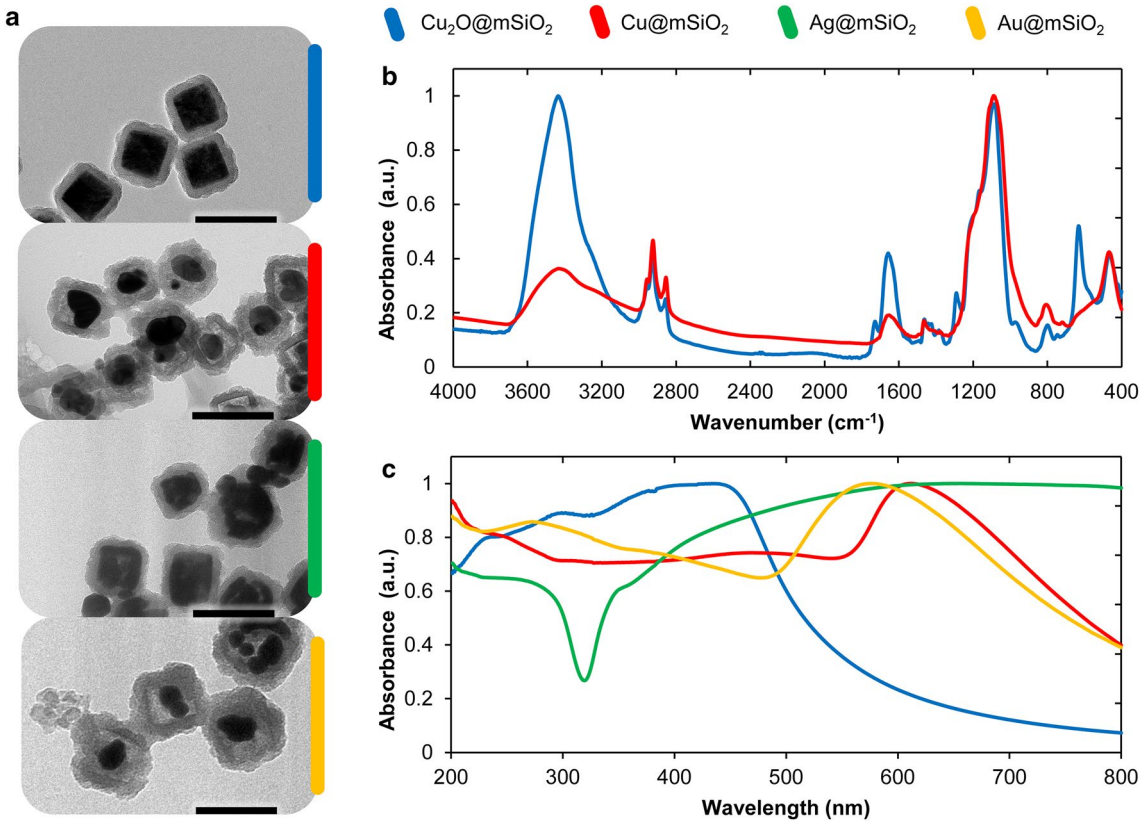

Fig. 4 **a** TEM images of $Cu_2O@mSiO_2$ (blue), $Cu@mSiO_2$ (red), $Ag@mSiO_2$ (green) and $Ag@mSiO_2$ (yellow). Scale bar 100 nm **b** IR spectroscopy before ($Cu_2O@mSiO_2$) and after ($Cu@mSiO_2$) liquid phase calcination demonstrating the removal of cuprous oide. **c** UV-Vis spectra displaying surface plasmon resonance peaks characteristic of metallic copper, silver and gold

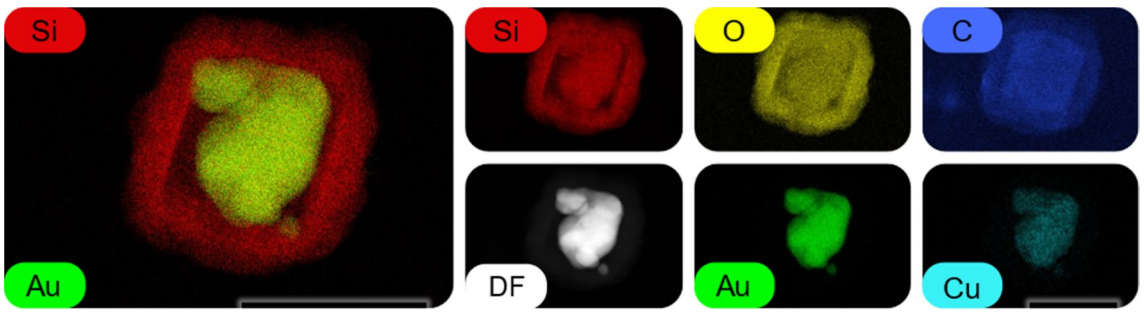

Fig. 5 TEM EDX elemental mapping of $Au@mSiO_2$. Scale bar 100 nm. EDX spectra available in SI.6

Since the copper cores are present in all $Cu@mSiO_2$ cubes, and can be readily accessed by reagents, they can function as seeds for further modification. Using galvanic replacement, it is possible to transform the copper cores into silver or gold. This transformation is visible from the change in UV–VIS spectra after galvanic replacement, Fig. 4c showing distinct UV–VIS absorption of both silver (green) and gold (yellow). Another indication of the successful galvanic replacement of copper with silver and gold, is the change in volume. Since the galvanic replacement follows standard half-reaction stoichiometry, as listed below in table 1, every three copper atoms are replaced by either two gold atoms or six silver atoms.

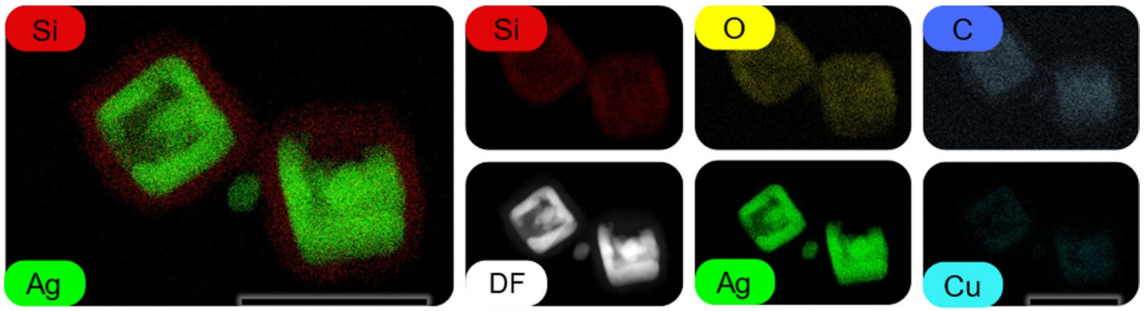

Fig. 6 TEM EDX elemental mapping of $Ag@mSiO_2$. Scale bar 100 nm. EDX spectra available in SI.6

The result is an increase in core volume after the galvanic replacement with silver and a decrease in core volume after replacement with gold, both visible in Fig. 4a.

Since the changes observed by TEM and UV–VIS are not conclusive whether the formed material is indeed silver or gold, energy-dispersive X-ray spectroscopy (EDX) was employed to determine the nature of the formed core. In Fig. 5, high angle annular dark field (HAADF/DF) micrographs of the particles after galvanic replacement with gold are shown in combination with EDX maps. The EDX signals of gold overlap with the core visible in HAADF, indicating the high-contrast material inside the cubes is indeed gold. Furthermore, EDX indicates that some trace amounts of copper are still present. Also, the EDX maps of Si and O are shown, which also coincide with the HAADF image of the low contrast silica shell. The carbon signal observed on the particle is speculated to be a result of adsorbed organic contaminants. The core-shell structure becomes apparent when the gold and silicon maps are combined, as visualized in Fig. 5, showing a clear silicium shell around the silver core. In Fig. 6, similar EDX maps of the particles obtained by the galvanic replacement with silver are presented, showing the same general features as the $Ag@mSiO_2$ particles. In contrast to the golden core, the silver core leaves a central void and covers the inner silica confinement, these shapes are not unusual for galvanic replacement and are attributed to the Kirkendall effect [50]. The noble nature of the gold core is confirmed via the traditional "acid test" and is discussed in SI.5.

3.3 Catalytic dye degradation

The functionality of the silver cores was assessed by the catalytic degradation of Congo red (Fig. 7). Congo red is readily hydrogenated by $NaBH_4$ in the presence of silver nanoparticles to colourless biphenyl and 4-amino-1-naphtalene-sulfonate [51]. Because Congo red degrades into colourless reaction

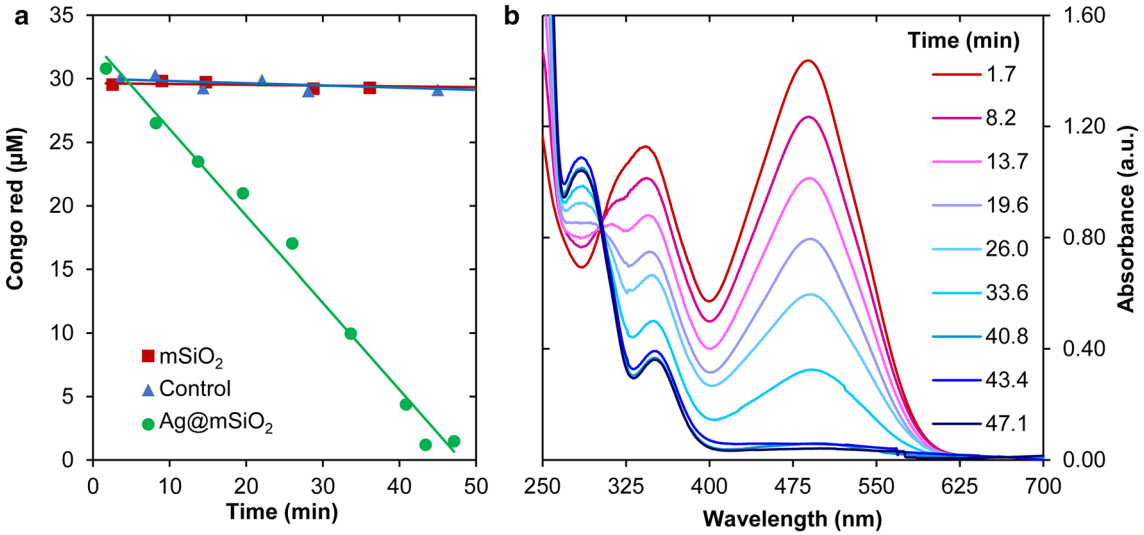

Fig. 7 **a** Congo red degradation rate with functional $Ag@mSiO_2$, empty void$@mSiO_2$ and a control without nanoparticles. **b** progression of UV–Vis spectrum during congo red degradation with $Ag@mSiO_2$. Note the isobestic point of the conversion at circa 300 nm. The degradation rate is further discussed in SI.7

products, the reaction is easily monitored by UV–VIS. After addition of $NaBH_4$, the $Ag@mSiO_2$ particles quickly discoloured the Congo red solution, resulting in very little absorption after 47 min (Fig. 7b). In Fig. 7a the Congo red concentration, determined from a calibration curve, is plotted against time for the dye degradation with $Ag@mSiO_2$, $mSiO_2$ shells, and without particles. It is clearly visible that the silver-containing nanocubes quickly degrade the dye, while the hollow mesoporous silica particles and the control (no particles) show only a slow degradation of Congo red. The spread in the data is likely caused by the production of gas bubbles in the cuvette by sodium borohydride, which interferes with the light-beam in the UV–VIS spectrophotometer.

4 Conclusions and outlook

Using a combination of liquid phase calcination and galvanic replacement it is possible to transform cuprous oxide – mesoporous silica core-shell nanocubes into nanocubes with functional cores. Cuprous oxide nanocubes are coated with mesoporous silica by using a micellar cetyltrimethylammonium bromide template. The thickness of the coating can be tuned between 10 and 70 nm by controlling the tetraethyl orthosilicate concentration in the reaction mixture. Nitrogen physisorption shows the colloidal cubic mesoporous silica shells to have a BET surface area of 1156 ± 17 m^2 g^{-1} and mesopores in the 2–3 nm range. With liquid phase calcination, the cubic cuprous oxide core is transformed in a spherical metallic copper core, which can be transformed into silver and gold using galvanic replacement reactions. Purely based on their standard potential, also other catalytically potent metals, such as platinum, palladium and rubidium, could potentially be used to replace the copper. [52] It is demonstrated that the silver core catalyzes the degradation of Congo red in the presence of sodium borohydride.

With a route to transform cubic core-shell particles into functional materials, it is possible to explore the deposition of different functional materials in the cubic void. Since galvanic replacement is limited to reductions with higher standard reaction potentials compared to the reduction of Cu^{2+}, ion exchange might offer a possibility to deposit materials other than noble metals. Another possible functionalization is by using the copper core as catalyst for controlled radical polymerization, which might allow the selective deposition of functional polymers in the voids.

Supplementary Information The online version contains supplementary material available at https://doi.org/10.1007/s10934-023-01471-x.

Acknowledgements Remco Dalebout is thanked for the measurement of, and useful discussionson, the adsorption isotherms. Hans Meeldijk is thanked for the HAADF and EDXimages. This project was funded by TTW (Toegepaste en Technische Wetenschappen)under project number 14210. Dr. Leon Bremer (DSM, now Nanoscolo), Dr. DamienReardon (DSM, now Covestro), Dr. Filip Oosterlinck (DSM) and Dr. Jurgen-Scheerder (DSM, now Covestro) from the Colloidal Mosaics project User Committeeare thanked for helpful discussions. NWO-TTW (Nederlandse Organisatie voor WetenschappelijkOnderzoek - Toegepaste en Technische Wetenschappen) is acknowledged forfinancial support.

Author contributions AJS: Writing—Original Draft, Conceptualization, Methodology, Investigation, Validation, Visualization. FD: Writing—Original Draft, Methodology, Investigation, Visualization. RTr: Writing—Review, Conceptualization, Funding acquisition, Supervision. APP: Writing—Review & Editing, Conceptualization, Funding acquisition, Supervision, Project administration.

Competing interests

The authors declare no competing interests.

Open Access This article is licensed under a Creative Commons Attribution 4.0 International License, which permits use, sharing, adaptation, distribution and reproduction in any medium or format, as long as you give appropriate credit to the original author(s) and the source, provide a link to the Creative Commons licence, and indicate if changes were made. The images or other third party material in this article are included in the article's Creative Commons licence, unless indicated otherwise in a credit line to the material. If material is not included in the article's Creative Commons licence and your intended use is not permitted by statutory regulation or exceeds the permitted use, you will need to obtain permission directly from the copyright holder. To view a copy of this licence, visit http://creativecommons.org/licenses/by/4.0/.

References

1. J.M. Meijer, A. Pal, S. Ouhajji, H.N. Lekkerkerker, A.P. Philipse, A.V. Petukhov, Observation of solid-solid transitions in 3D crystals of colloidal superballs. Nat. Commun. **8**, 14352 (2017). https://doi.org/10.1038/ncomms14352
2. J. Henzie, M. Grunwald, A. Widmer-Cooper, P.L. Geissler, P. Yang, Self-assembly of uniform polyhedral silver nanocrystals into densest packings and exotic superlattices. Nat. Mater. **11**(2), 131–137 (2011). https://doi.org/10.1038/nmat3178
3. L. Rossi, S. Sacanna, W.T.M. Irvine, P.M. Chaikin, D.J. Pine, A.P. Philipse, Cubic crystals from cubic colloids. Soft Matter **7**(9), 4139–4142 (2011). https://doi.org/10.1039/c0sm01246g
4. J.W.J. De Folter, E.M. Hutter, S.I.R. Castillo, K.E. Klop, A.P. Philipse, W.K. Kegel, Particle shape anisotropy in Pickering Emulsions: Cubes and Peanuts. Langmuir **30**(4), 955–964 (2014). https://doi.org/10.1021/la402427q
5. J.S. van der Burgt, J.J. Geuchies, B. van der Meer, H. Vanrompay, D. Zanaga, Y. Zhang, W. Albrecht, A.V. Petukhov, L. Filion, S. Bals, I. Swart, D. Vanmaekelbergh, Cuboidal Supraparticles Self-Assembled from cubic CsPbBr3 Perovskite Nanocrystals. J. Phys. Chem. C Nanomater Interfaces **122**(27), 15706–15712 (2018). https://doi.org/10.1021/acs.jpcc.8b02699
6. D. Wang, M. Hermes, R. Kotni, Y. Wu, N. Tasios, Y. Liu, B. de Nijs, E.B. van der Wee, C.B. Murray, M. Dijkstra, A. van Blaaderen, Interplay between spherical confinement and particle shape on the self-assembly of rounded cubes. Nat Commun (2018). https://doi.org/10.1038/s41467-018-04644-4
7. Y. Sun, Y. Xia, Shape-controlled synthesis of gold and silver nanoparticles. Science **298**(5601), 2176–2179 (2002). https://doi.org/10.1126/science.1077229

8. K.M. Bratlie, H. Lee, K. Komvopoulos, P. Yang, G.A. Somorjai, Platinum nanoparticle shape Effects on Benzene Hydrogenation selectivity. Nano Lett **7**(10), 3097–3101 (2007). https://doi.org/10.1021/nl0716000
9. S.E. Skrabalak, J. Chen, L. Au, X. Lu, X. Li, Y. Xia, Gold Nanocages for Biomedical Applications. Adv. Mater **19**(20), 3177–3184 (2007). https://doi.org/10.1002/adma.200701972
10. L. Gou, C.J. Murphy, Solution-phase synthesis of Cu2O nanocubes. Nano Lett **3**(2), 231–234 (2003). https://doi.org/10.1021/nl0258776
11. D. Kim, N. Lee, M. Park, B.H. Kim, K. An, T. Hyeon, Synthesis of Uniform Ferrimagnetic Magnetite Nanocubes. J. Am. Chem. Soc **131**(2), 454–455 (2009). https://doi.org/10.1021/ja8086906
12. P. Ramasamy, D.H. Lim, B. Kim, S.H. Lee, M.S. Lee, J.S. Lee, All-inorganic cesium lead halide perovskite nanocrystals for photodetector applications. Chem. Commun. (Camb) **52**(10), 2067–2070 (2016). https://doi.org/10.1039/c5cc08643d
13. A. Tao, P. Sinsermsuksakul, P. Yang, Polyhedral Silver Nanocrystals with distinct scattering signatures. Angew. Chem. Int. Ed **45**(28), 4597–4601 (2006). https://doi.org/10.1002/anie.200601277
14. N. Hijnen, D. Cai, P.S. Clegg, Bijels stabilized using rod-like particles. Soft Matter **11**(22), 4351–4355 (2015). https://doi.org/10.1039/c5sm00265f
15. M.A. Khan, A.J. Sprockel, K.A. Macmillan, M.T. Alting, S.P. Kharal, S. Boakye-Ansah, M.F. Haase, Nanostructured, Fluid-Bicontinuous gels for Continuous-Flow liquid–liquid extraction. Adv Mater (2022). https://doi.org/10.1002/adma.202109547
16. C. Liu, J. Li, J. Qi, J. Wang, R. Luo, J. Shen, X. Sun, W. Han, L. Wang, Yolk–Shell Fe0@SiO2 Nanoparticles as Nanoreactors for Fenton-like Catalytic reaction. ACS Appl. Mater. Interfaces **6**(15), 13167–13173 (2014). https://doi.org/10.1021/am503063m
17. M. Xiao, C. Zhao, H. Chen, B. Yang, J. Wang (2012) ShipinaBottle Growth of Noble Metal Nanostructures. Adv Funct Mater. 22(21): 4526–4532.
18. S.I.R. Castillo, *Cubic Colloids; Synthesis, Functionalization and Applications* (Utrecht, Utrecht University, 2015)
19. F. Dekker, R. Tuinier, A.P. Philipse, Synthesis of hollow silica nanocubes with tuneable size and shape, suitable for light scattering studies. Colloids Interf (2018). https://doi.org/10.3390/colloids2040044
20. J. Liu, S.Z. Qiao, J.S. Chen, X.W. Lou, X. Xing, G.Q. Lu, Yolk/shell nanoparticles: new platforms for nanoreactors, drug delivery and lithium-ion batteries. Chem. Commun **47**(47), 12578–12591 (2011). https://doi.org/10.1039/C1CC13658E
21. J. Feng, Y. Yin, Self-templating approaches to Hollow Nanostructures. Adv. Mater (2019). https://doi.org/10.1002/adma.201802349
22. R. Ghosh Chaudhuri, S. Paria, Core/Shell Nanoparticles: classes, Properties, synthesis mechanisms, characterization, and applications. Chem. Rev **112**(4), 2373–2433 (2012). https://doi.org/10.1021/cr100449n
23. Y. Bao, C. Shi, T. Wang, X. Li, J. Ma, Recent progress in hollow silica: template synthesis, morphologies and applications. Microporous Mesoporous Mater **227**, 121–136 (2016). https://doi.org/10.1016/j.micromeso.2016.02.040
24. Y. Sun, Y. Xia, Mechanistic study on the replacement reaction between silver nanostructures and Chloroauric Acid in Aqueous Medium. J. Am. Chem. Soc **126**(12), 3892–3901 (2004). https://doi.org/10.1021/ja039734c
25. X. Wei, Q. Fan, H. Liu, Y. Bai, L. Zhang, H. Zheng, Y. Yin, C. Gao, Holey Au–Ag alloy nanoplates with built-in hotspots for surface-enhanced Raman scattering. Nanoscale **8**(34), 15689–15695 (2016). https://doi.org/10.1039/c6nr04866h
26. T.-S. Deng, J.E.S. van der Hoeven, A.O. Yalcin, H.W. Zandbergen, M.A. van Huis, A. van Blaaderen, Oxidative etching and metal overgrowth of gold nanorods within mesoporous silica shells. Chem. Mater **27**(20), 7196–7203 (2015). https://doi.org/10.1021/acs.chemmater.5b03749
27. W. Albrecht, J.E.S. Van Der Hoeven, T.-S. Deng, P.E. De Jongh, A. Van Blaaderen, Fully alloyed metal nanorods with highly tunable properties. Nanoscale **9**(8), 2845–2851 (2017). https://doi.org/10.1039/c6nr08484b
28. S.I.R. Castillo, S. Ouhajji, S. Fokker, B.H. Erné, C.T.W.M. Schneijdenberg, D.M.E. Thies-Weesie, A.P. Philipse, Silica cubes with tunable coating thickness and porosity: from hematite filled silica boxes to hollow silica bubbles. Microporous Mesoporous Mater **195**, 75–86 (2014). https://doi.org/10.1016/j.micromeso.2014.03.047
29. X. Zhang, Z. Xi, J.O.A. Machuki, J. Luo, D. Yang, J. Li, W. Cai, Y. Yang, L. Zhang, J. Tian, K. Guo, Y. Yu, F. Gao, Gold cube-in-cube based Oxygen Nanogenerator: a theranostic nanoplatform for modulating Tumor Microenvironment for Precise Chemo-Phototherapy and Multimodal Imaging. ACS Nano **13**(5), 5306–5325 (2019). https://doi.org/10.1021/acsnano.8b09786
30. S. Xiao, L. Hu, X. Pang, S. Li, Synthesis of a Novel Mesoporous Carbon Nanocube@Mesoporous Silica@Poly(acrylic acid) composite and application as potential drug carriers. Russ. J. Phys. Chem. A **93**(7), 1349–1356 (2019). https://doi.org/10.1134/S003602441907029X
31. S.I.R. Castillo, C.E. Pompe, J. van Mourik, D.M.A. Verbart, D.M.E. Thies-Weesie, P.E. de Jongh, A.P. Philipse, Colloidal cubes for the enhanced degradation of organic dyes. J. Mater. Chem. A **2**(26), 10193–10201 (2014). https://doi.org/10.1039/C4TA01373E
32. M. Zhang, K. Fang, M. Lin, B. Hou, L. Zhong, Y. Zhu, W. Wei, Y. Sun, Controlled fabrication of Iron Oxide/Mesoporous silica Core–Shell Nanostructures. J. Phys. Chem. C **117**(41), 21529–21538 (2013). https://doi.org/10.1021/jp4049583
33. Z.-Y. Yuan, B.-L. Su, Insights into hierarchically meso–macroporous structured materials. J. Mater. Chem **16**(7), 663–677 (2006). https://doi.org/10.1039/B512304F
34. J. Li, X. Liang, J.B. Joo, I. Lee, Y. Yin, F. Zaera, Mass Transport across the porous oxide shells of Core–Shell and Yolk–Shell Nanostructures in Liquid Phase. J. Phys. Chem. C **117**(39), 20043–20053 (2013). https://doi.org/10.1021/jp406991y
35. J.Y. Ying, C.P. Mehnert, M.S. Wong, 1999 *S*ynthesis and Applications of Supramolecular-Templated Mesoporous Materials. Angewandte Chemie International Edition 38(2): 56–77
36. C.T. Kresge, M.E. Leonowicz, W.J. Roth, J.C. Vartuli, J.S. Beck, Ordered mesoporous molecular sieves synthesized by a liquid-crystal template mechanism. Nature **359**(6397), 710–712 (1992). https://doi.org/10.1038/359710a0
37. M. Liong, J. Lu, M. Kovochich, T. Xia, S.G. Ruehm, A.E. Nel, F. Tamanoi, J.I. Zink, Multifunctional inorganic nanoparticles for imaging, targeting, and Drug Delivery. ACS Nano **2**(5), 889–896 (2008). https://doi.org/10.1021/nn800072t
38. K. Deekamwong, J. Wittayakun, Template removal by ion-exchange extraction from siliceous MCM-41 synthesized by microwave-assisted hydrothermal method. Microporous Mesoporous Mater **239**, 54–59 (2017). https://doi.org/10.1016/j.micromeso.2016.09.049
39. V. Cauda, C. Argyo, D.G. Piercey, T. Bein, "Liquid-phase calcination" of colloidal mesoporous silica nanoparticles in high-boiling solvents. J Am Chem Soci **133**(17), 6484–6486 (2011). https://doi.org/10.1021/ja1067492
40. J.C. Park, J. Kim, H. Kwon, H. Song, Gram-scale synthesis of Cu2O nanocubes and subsequent oxidation to CuO Hollow Nanostructures for Lithium-Ion Battery Anode materials. Adv. Mater **21**(7), 803–807 (2009). https://doi.org/10.1002/adma.200800596

41. J. Jiang, S.-H. Kim, L. Piao, The facile synthesis of Cu@SiO2 yolk–shell nanoparticles via a disproportionation reaction of silica-encapsulated Cu2O nanoparticle aggregates. Nanoscale **7**(18), 8299–8303 (2015). https://doi.org/10.1039/C5NR01484K
42. I.E. Stewart, S. Ye, Z. Chen, P.F. Flowers, B.J. Wiley, Synthesis of Cu–Ag, Cu–Au, and Cu–Pt Core–Shell Nanowires and their use in Transparent conducting Films. Chem. Mater **27**(22), 7788–7794 (2015). https://doi.org/10.1021/acs.chemmater.5b03709
43. M. Thommes, K. Kaneko, A.V. Neimark, J.P. Olivier, F. Rodriguez-Reinoso, J. Rouquerol, K.S.W. Sing, Physisorption of gases, with special reference to the evaluation of surface area and pore size distribution (IUPAC Technical Report). Pure Appl Chem **87**(9–10), 1051–1069 (2015). https://doi.org/10.1515/pac-2014-1117
44. H. Yang, Y. Min, Y. Kim, U. Jeong, Preparation of Cu2O@SiO2 particles and their evolution to hollow SiO2 particles. Colloids Surf., A **420**, 30–36 (2013). https://doi.org/10.1016/j.colsurfa.2012.12.016
45. J.C. Groen, L.A.A. Peffer, J. Pérez-Ramírez, Pore size determination in modified micro- and mesoporous materials. Pitfalls and limitations in gas adsorption data analysis. Microporous Mesoporous Mater **60**(1), 1–17 (2003). https://doi.org/10.1016/S1387-1811(03)00339-1
46. D.W. Zhao, Y.; Zhou, Wuzong, *Ordered Mesoporous Materials* (Wiley-VCH, Weinheim, 2013)
47. L. Gao, C. Pang, D. He, L. Shen, A. Gupta, N. Bao, Synthesis of hierarchical nanoporous Microstructures via the Kirkendall Effect in Chemical reduction process. Rep Sci (2015). https://doi.org/10.1038/srep16061
48. J.A. Creighton, D.G. Eadon, Ultraviolet–visible absorption spectra of the colloidal metallic elements. J. Chem. Soc., Faraday Trans **87**(24), 3881–3891 (1991). https://doi.org/10.1039/FT9918703881
49. D.W. Ball, *Physical Chemistry; Standard potentials, Chap. 8, page 232*. Second Edition ed. 2002: Wadsworth
50. S.W. Chee, S.F. Tan, Z. Baraissov, M. Bosman, U. Mirsaidov, Direct observation of the nanoscale Kirkendall effect during galvanic replacement reactions. Nat Commun (2017). https://doi.org/10.1038/s41467-017-01175-2
51. R. Rajesh, S.S. Kumar, R. Venkatesan, Efficient degradation of azo dyes using ag and au nanoparticles stabilized on graphene oxide functionalized with PAMAM dendrimers. New J. Chem **38**(4), 1551–1558 (2014). https://doi.org/10.1039/C3NJ01050C
52. S.M. Alia, Y.S. Yan, B.S. Pivovar, Galvanic displacement as a route to highly active and durable extended surface electrocatalysts. Catal. Sci. Technol. **4**(10), 3589–3600 (2014). https://doi.org/10.1039/c4cy00736k

Publisher's Note Springer Nature remains neutral with regard to jurisdictional claims in published maps and institutional affiliations.